Large-scale high aspect ratio Al-doped ZnO nanopillars arrays as anisotropic metamaterials.

Shkondin, Evgeniy; Takayama, Osamu; Panah, Mohammad Esmail Aryaee; Liu, Pei; Larsen, Pernille Voss; Mar, Mikkel Dysseholm; Jensen, Flemming; Lavrinenko, Andrei

Published in:
Optical Materials Express

Link to article, DOI:
10.1364/OME.7.001606

Publication date:
2017

Document Version
Publisher's PDF, also known as Version of record

Research Article | Vol. 7, No. 5 | 1 May 2017 | OPTICAL MATERIALS EXPRESS 1606

Optical Materials EXPRESS

Large-scale high aspect ratio Al-doped ZnO nanopillars arrays as anisotropic metamaterials

E. SHKONDIN,[1,2,*] O. TAKAYAMA,[2] M. E. ARYAEE PANAH,[2] P. LIU,[3] P. V. LARSEN,[1] M. D. MAR,[1] F. JENSEN,[1] AND A. V. LAVRINENKO[2]

[1]*National Center for Micro- and Nanofabrication (DANCHIP), DK-2800 Kongens Lyngby, Denmark*
[2]*Department of Photonics Engineering, Technical University of Denmark, DK-2800 Kongens Lyngby, Denmark*
[3]*Center for Electron Nanoscopy (CEN), Technical University of Denmark, DK-2800 Kongens Lyngby, Denmark*
**eves@fotonik.dtu.dk*

Abstract: High aspect ratio free-standing Al-doped ZnO (AZO) nanopillars and nanotubes were fabricated using a combination of advanced reactive ion etching and atomic layer deposition (ALD) techniques. Prior to the pillar and tube fabrication, AZO layers were grown on flat silicon and glass substrates with different Al concentrations at 150-250 °C. For each temperature and Al concentration the ALD growth behavior, crystalline structure, physical, electrical and optical properties were investigated. It was found that AZO films deposited at 250 °C exhibit the most pronounced plasmonic behavior with the highest plasma frequency. During pillar fabrication, AZO conformally passivates the silicon template, which is characteristic of typical ALD growth conditions. The last step of fabrication is heavily dependent on the selective chemistry of the SF_6 plasma. It was shown that silicon between AZO structures can be selectively removed with no observable influence on the ALD deposited coatings. The prepared free-standing AZO structures were characterized using Fourier transform infrared spectroscopy (FTIR). The restoration of the effective permittivities of the structures reveals that their anisotropy significantly deviates from the effective medium approximation (EMA) prognoses. It suggests that the permittivity of the AZO in tightly confined nanopillars is very different from that of flat AZO films.

OCIS codes: (160.3918) Metamaterials; (160.4760) Optical properties; (240.0310) Thin films; (220.4241) Nanostructure fabrication.

References and links

1. K. Nomura, H. Ohta, A. Takagi, T. Kamiya, M. Hirano, and H. Hosono, "Room-temperature fabrication of transparent flexible thin-film transistors using amorphous oxide semiconductors," Nature **432**(7016), 488–492 (2004).
2. O. K. Varghese, M. Paulose, and C. A. Grimes, "Long vertically aligned titania nanotubes on transparent conducting oxide for highly efficient solar cells," Nat. Nanotechnol. **4**(9), 592–597 (2009).
3. D.-J. Lee, H.-M. Kim, J.-Y. Kwon, H. Choi, S.-H. Kim, and K.-B. Kim, "Structural and Electrical Properties of Atomic Layer Deposited Al-Doped ZnO Films," Adv. Funct. Mater. **21**(3), 448–455 (2011).
4. H. Kim, C. M. Glimore, A. Piqué, J. S. Horwitz, H. Mattoussi, H. Murata, Z. H. Kafafi, and D. B. Chrisey, "Electrical, optical, and structural properties of indium–tin–oxide thin films for organic light-emitting devices," J. Appl. Phys. **86**(11), 6451–6461 (1999).
5. P. Banerjee, W.-J. Lee, K. Bae, S. B. Lee, and G. W. Rubloff, "Structural, electrical, and optical properties of atomic layer deposition Al-doped ZnO films," J. Appl. Phys. **108**(4), 043504 (2010).
6. T. Dhakal, D. Vanhart, R. Christian, A. Nandur, A. Sharma, and C. R. Westgate, "Growth morphology and electrical/optical properties of Al-doped ZnO thin films grown by atomic layer deposition," J. Vac. Sci. Technol. A **30**(2), 021202 (2012).
7. Y. Geng, Z.-Y. Xie, S.-S. Xu, Q.-Q. Sun, S.-J. Ding, H.-L. Lu, and D. W. Zhang, "Effects of Rapid Thermal Annealing on Structural, Luminescent, and Electrical Properties of Al-Doped ZnO Films Grown by Atomic Layer Deposition," ECS J. Solid State Sci. Technol. **1**(3), N45–N48 (2012).
8 T. Tynell, H. Yamauchi, M. Karppinen, R. Okazaki, and I. Terasaki, "Atomic layer deposition of Al-doped ZnO thin films," J. Vac. Sci. Technol. A **31**, 01A109 (2013).

#289092 https://doi.org/10.1364/OME.7.001606
Journal © 2017 Received 6 Mar 2017; revised 10 Apr 2017; accepted 11 Apr 2017; published 13 Apr 2017

Optical Materials EXPRESS

9. E. B. Pollock and R. J. Lad, "Influence of dosing sequence and film thickness on structure and resistivity of Al-ZnO films grown by atomic layer deposition," J. Vac. Sci. Technol. A **32**(4), 041516 (2014).
10. A. Crovetto, T. S. Ottsen, E. Stamate, D. Kjær, J. Schou, and O. Hansen, "On performance limitations and property correlations of Al-doped ZnO deposited by radio-frequency sputtering," J. Phys. D Appl. Phys. **49**(29), 295101 (2016).
11. G. V. Naik, J. Liu, A. V. Kildishev, V. M. Shalaev, and A. Boltasseva, "Demonstration of Al:ZnO as a plasmonic component for near-infrared metamaterials," Proc. Natl. Acad. Sci. U.S.A. **109**(23), 8834–8838 (2012).
12. A. K. Pradhan, R. M. Mundle, K. Santiago, J. R. Skuza, B. Xiao, K. D. Song, M. Bahoura, R. Cheaito, and P. E. Hopkins, "Extreme tunability in aluminum doped zinc oxide plasmonic materials for near-infrared applications," Sci. Rep. **4**, 6415 (2014).
13. C. T. Riley, J. S. T. Smalley, K. W. Post, D. N. Basov, Y. Fainman, D. Wang, Z. Liu, and D. J. Sirbuly, "High-Quality, Ultraconformal Aluminum-Doped Zinc Oxide Nanoplasmonic and Hyperbolic Metamaterials," Small **12**(7), 892–901 (2016).
14. S. Y. Myong, S. J. Baik, C. H. Lee, W. Y. Cho, and K. S. Lim, "Extremely transparent and conductive ZnO:Al thin films prepared by photo-assisted metalorganic chemical vapor deposition (photo-MOCVD) using AlCl3(6H2O) as new doping material," Jpn. J. Appl. Phys. **36**(8), 1078–1081 (1997).
15. P. P. Sahay and R. K. Nath, "Al-doped ZnO thin films as methanol sensors," Sens. Actuators B Chem. **134**(2), 654–659 (2008).
16. H. Tanaka, K. Ihara, T. Miyata, H. Sato, and T. Minami, "Low resistivity polycrystalline ZnO : Al thin films prepared by pulsed laser deposition," J. Vac. Sci. Technol. A **22**(4), 1757–1762 (2004).
17. S.-K. Kim and J.-Y. Son, "Epitaxial ZnO Thin Films for the Application of Ethanol Gas Sensor: Thickness and Al-Doping Effects," Electrochem. Solid-State Lett. **12**(2), J17–J19 (2009).
18. S. M. George, "Atomic layer deposition: an overview," Chem. Rev. **110**(1), 111–131 (2010).
19. S. Law, V. Podolskiy, and D. Wasserman, "Towards nano-scale photonics with micro-scale photons: the opportunities and challenges of mid-infrared plasmonics," Nanophotonics **2**(2), 103–130 (2013).
20. Y. Zhong, S. D. Malagari, T. Hamilton, and D. Wasserman, "Review of mid-infrared plasmonic materials," J. Nanophotonics **9**(1), 093791 (2015).
21. J. Haas and B. Mizaikoff, "Advances in mid-infrared spectroscopy for chemical analysis," Annu. Rev. Anal. Chem. (Palo Alto, Calif.) **9**(1), 45–68 (2016).
22. P. R. West, S. Ishii, G. V. Naik, N. K. Emani, V. M. Shalaev, and A. Boltasseva, "Searching for better plasmonic materials," Laser Photonics Rev. **4**(6), 795–808 (2010).
23. A. Boltasseva, "Empowering plasmonics and metamaterials technology with new material platforms," MRS Bull. **39**(5), 461–468 (2014).
24. V. N'Tsame Guilengui, L. Cerutti, J. B. Rodriguez, E. Tournié, and T. Taliercio, "Localized surface plasmon resonances in highly doped semiconductors nanostructures," Appl. Phys. Lett. **101**(16), 161113 (2012).
25. M. Cada, D. Blazek, J. Pistora, K. Postava, and P. Siroky, "Theoretical and experimental study of plasmonic effects in heavily doped gallium arsenide and indium phosphide," Opt. Mater. Express **5**(2), 340–352 (2015).
26. M. E. Panah, O. Takayama, S. V. Morozov, K. E. Kudryavtsev, E. S. Semenova, and A. V. Lavrinenko, "Highly doped InP as a low loss plasmonic material for mid-IR region," Opt. Express **24**(25), 29077–29088 (2016).
27. J. Sun, N. M. Litchinitser, and J. Zhou, "Indefinite by Nature: From Ultraviolet to Terahertz," ACS Photonics **1**(4), 293–303 (2014).
28. J. D. Caldwell, I. Vurgaftman, J. G. Tischler, O. J. Glembocki, J. C. Owrutsky, and T. L. Reinecke, "Atomic-scale photonic hybrids for mid-infrared and terahertz nanophotonics," Nat. Nanotechnol. **11**(1), 9–15 (2016).
29. W. Cai and V. Shalaev, *Optical Metamaterials* (Springer, 2010).
30. S. Jahani and Z. Jacob, "All-dielectric metamaterials," Nat. Nanotechnol. **11**(1), 23–36 (2016).
31. P. Shekhar, J. Atkinson, and Z. Jacob, "Hyperbolic metamaterials: fundamentals and applications," Nano Converg **1**(1), 14 (2014).
32 Y. Guo, W. Newman, C. L. Cortes, and Z. Jacob, "Applications of Hyperbolic Metamaterial Substrates," Adv. Optoelectron. **2012**(2012), 452502 (2012).
33. L. Ferrari, C. Wu, D. Lepage, X. Zhang, and Z. Liu, "Hyperbolic metamaterials and their applications," Prog. Quantum Electron. **40**, 1–40 (2015).
34. D. Lu and Z. Liu, "Hyperlenses and metalenses for far-field super-resolution imaging," Nat. Commun. **3**, 1205 (2012).
35. A. V. Kabashin, P. Evans, S. Pastkovsky, W. Hendren, G. A. Wurtz, R. Atkinson, R. Pollard, V. A. Podolskiy, and A. V. Zayats, "Plasmonic nanorod metamaterials for biosensing," Nat. Mater. **8**(11), 867–871 (2009).
36. K. V. Sreekanth, Y. Alapan, M. ElKabbash, E. Ilker, M. Hinczewski, U. A. Gurkan, A. De Luca, and G. Strangi, "Extreme sensitivity biosensing platform based on hyperbolic metamaterials," Nat. Mater. **15**(6), 621–627 (2016).
37. S. Molesky, C. J. Dewalt, and Z. Jacob, "High temperature epsilon-near-zero and epsilon-near-pole metamaterial emitters for thermophotovoltaics," Opt. Express **21**(1), A96–A110 (2013).
38. S. S. Kruk, Z. J. Wong, E. Pshenay-Severin, K. O'Brien, D. N. Neshev, Y. S. Kivshar, and X. Zhang, "Magnetic hyperbolic optical metamaterials," Nat. Commun. **7**, 11329 (2016).
39. A. A. High, R. C. Devlin, A. Dibos, M. Polking, D. S. Wild, J. Perczel, N. P. de Leon, M. D. Lukin, and H. Park, "Visible-frequency hyperbolic metasurface," Nature **522**(7555), 192–196 (2015).

Optical Materials EXPRESS

40. Y. Huang, G. Pandraud, and P. M. Sarro, "The atomic layer deposition array defined by etch-back technique: a new method to fabricate TiO2 nanopillars, nanotubes and nanochannel arrays," Nanotechnology **23**(48), 485306 (2012).
41. E. Shkondin, O. Takayama, J. M. Lindhard, P. V. Larsen, M. D. Mar, F. Jensen, and A. V. Lavrinenko, "Fabrication of high aspect ratio TiO_2 and Al_2O_3 nanogratings by atomic layer deposition," J. Vac. Sci. Technol. A **34**(3), 31605 (2016).
42. Q. Hou, F. Meng, and J. Sun, "Electrical and optical properties of Al-doped ZnO and ZnAl2O4 films prepared by atomic layer deposition," Nanoscale Res. Lett. **8**(1), 144 (2013).
43. P. Zaumseil, "High-resolution characterization of the forbidden Si 200 and Si 222 reflections," J. Appl. Cryst. **48**(Pt 2), 528–532 (2015).
44. M. Birkholz, "Thin Film Analysis by X-Ray Scattering," in *X-Ray Spectrometry* (Wiley, 2005), chap. 3.
45. M. Latzel, M. Göbelt, G. Brönstrup, C. Venzago, S. W. Schmitt, G. Sarau, and S. H. Christiansen, "Modeling the dielectric function of degenerately doped ZnO: Al thin films grown by ALD using physical parameters," Opt. Mater. Express **5**(9), 1979–1990 (2015).
46. P. Kelly, M. Liu, and L. Kuznetsova, "Designing optical metamaterial with hyperbolic dispersion based on an Al:ZnO/ZnO nano-layered structure using the atomic layer deposition technique," Appl. Opt. **55**(11), 2993–2997 (2016).
47. J. Tauc, "Optical properties and electronic structure of amorphous Ge and Si," Mater. Res. Bull. **3**(1), 37–46 (1968).
48. E. Burstein, "Anomalous optical absorption limit in InSb," Phys. Rev. **93**(3), 632–633 (1954).
49. T. S. Moss, "The interpretation of the properties of indium antimonide," Proc. Phys. Soc. Lond. **67B**(10), 775–782 (1954).
50. C. J. Gabriel and A. Nedoluha, "Transmittance and reflectance of systems of thin and thick layers," Opt. Acta Int. J. Opt. **18**(6), 415–423 (1971).
51. W. H. Press, S. A. Teukolsky, W. T. Vetterling, and B. P. Flannery, *Numerical Recipes: The Art of Scientific Computing* (Cambridge University Press, 2007).
52. R. Kitamura, L. Pilon, and M. Jonasz, "Optical constants of silica glass from extreme ultraviolet to far infrared at near room temperature," Appl. Opt. **46**(33), 8118–8133 (2007).
53. Y. Wang, A. Capretti, and L. Dal Negro, "Wide tuning of the optical and structural properties of alternative plasmonic materials," Opt. Mater. Express **5**(11), 2415–2430 (2015).
54. S. Prayakarao, S. Robbins, N. Kinsey, A. Boltasseva, V. M. Shalaev, U. B. Wiesner, C. E. Bonner, R. Hussain, N. Noginova, and M. A. Noginov, "Gyroidal titanium nitride as nonmetallic metamaterial," Opt. Mater. Express **5**(6), 1316–1322 (2015).
55. D. Artigas and L. Torner, "Dyakonov surface waves in photonic metamaterials," Phys. Rev. Lett. **94**(1), 013901 (2005).
56. S. Lin, H. Tang, Z. Ye, H. He, Y. Zheng, B. Zhao, and L. Zhu, "Synthesis of vertically aligned Al-doped ZnO nanorods array with controllable Al concentration," Mater. Lett. **62**(4–5), 603–606 (2008).

1. Introduction

Transparent conductive oxides (TCOs) are important materials within optical physics and engineering [1–3]. Among them, indium tin oxide is the most investigated and implemented compound [4]. However, it has disadvantages including toxicity and the cost of indium. Recent development on alternative TCOs has revealed that Al-doped ZnO (AZO) can become a promising replacement [5–10]. Additionally, AZO has peculiar optical properties, *e.g.* plasmonic response in the near and mid-infrared (mid-IR) region [11–13] and tunability by adjusting the doping level. This makes AZO an advantageous and promising alternative plasmonic material, having a wide range of tunable optical and electrical properties.

A variety of deposition methods exist for the preparation of AZO. These include RF magnetron sputtering [10], chemical vapor deposition [14], chemical spray pyrolysis [15], pulsed laser deposition [16,17] and atomic layer deposition (ALD) [5–9]. Specifically, ALD technology is important since it is the only technique allowing conformal and uniform deposition of both metallic and dielectric layers on surfaces with advanced topologies, such as pores, trenches, holes, *etc* [18]. ALD also presents advantages such as low-temperature growth, precise thickness and composition control. For these reasons, ALD grown AZO films have been heavily studied in the last decade for their physical properties.

Plasmonics in the mid-IR regime offers various unique applications such as thermal imaging and biosensing applications [19,20]. Especially, mid-IR spectroscopy in the wavelength range of 2.5–20 μm (4,000 cm^{-1} to 500 cm^{-1}) provides specific chemical and compositional information in the gas, liquid, and solid phases owing to molecules vibrational

Optical Materials EXPRESS

and rotational absorption bands, thus enabling a wide variety of sensing applications in industrial production monitoring, materials science, biotechnology, detection of toxic gases and liquids, environmental analysis, medicine, and medical diagnostics [21]. Traditionally, noble metals are used as plasmonic materials due to their abundant free electrons in the conductance band. However, their large permittivity, especially in the infrared range, results in high loss and weak confinement to the surface. Therefore, the quest for alternative materials suitable for a certain wavelength range in the vast mid-IR region has been the focus of research in last several years. Consequently, various plasmonic alternatives have been investigated: transparent conductive oxides [22,23], heavily doped III-V semiconductors [24–26], polar materials [27], 2D materials (graphene, hBN, etc.) [28]. Each group of alternatives has its own preferential operating wavelength regime due to the available free carrier concentrations and mobilities. The wide tunability of AZO favors its employment in optical metamaterials, exhibiting large anisotropy, epsilon-near-zero regime and hyperbolic dispersion [11,13].

Optical metamaterials are artificially engineered composites of different components and designed optical properties beyond those available in nature [29,30]. Metamaterials with hyperbolic dispersion or hyperbolic metamaterials (HMMs) are the class of electromagnetic subwavelength structures which can be described by a dielectric permittivity tensor ε with components of opposite signs (*e.g.* $\varepsilon_x = \varepsilon_y > 0$, $\varepsilon_z < 0$) allowing the existence of hyperbolic iso-frequency contours in the wavevector space [31]. Characteristically, hyperbolic metamaterials (HMMs) possess unusually high wavevectors, enlarged optical density of states, and extreme anisotropy, leading to wide variety of potential applications such as the broadband enhancement of spontaneous emission for a single photon source [32,33], sub-wavelength imaging [34], sensing [35,36], thermal engineering [37,38] and steering of optical signals [39]. One of the principal geometries that support hyperbolic behavior is the so-called wire medium, e.g. an anisotropic composite of metallic pillars incorporated in a dielectric host matrix.

The purpose of this work is to investigate physical and optical properties of AZO thin films and 2D arrays of vertically arranged nanostructures (pillars or tubes) in order to test the anisotropy achievable in pillars array. Fabrication of pillars was carried out in a combination of ALD with advanced deep reactive ion etching (DRIE). A similar technique has been implemented previously in the fabrication of photonic crystals made of TiO_2 [40] and more recent in the fabrication of high aspect ratio Al_2O_3 and TiO_2 trenches [41]. The method is based on ALD deposition on Si structures with a sub-sequential removal of silicon. The use of ALD in combination with a sacrificial silicon mold is a novel way to create large-scale high aspect ratio metal oxides structures of exceptional quality. The success of this procedure is heavily dependent on the ability to etch silicon selectively without affecting the ALD coatings. Conventionally, silicon dry etching is based on SF_6 process gas. It has been shown that silicon can be removed selectively without any influence on the ALD deposited Al_2O_3 and TiO_2 [40,41]. This work demonstrates that ZnO-based coatings can also be patterned by the same procedure. The excellent selectivity is demonstrated in fabrication of 20 nm thin free-standing AZO tubes. Optical characterization by Fourier transform infrared spectroscopy (FTIR) shows that the fabricated pillar structures have positive effective permittivities in the wavelength range of 2 – 20 μm. Moreover, the retrieved effective permittivities do not behave as predicted by the effective medium theory, indicating that AZO in nanopillars has different dielectric functions compared to the flat film and exhibit greatly reduced plasmonic properties.

2. Fabrication and characterization of AZO thin films

Prior to metamaterial fabrication, ALD growth conditions with different Al concentrations were investigated by growing 100 nm thick AZO thin films on flat silicon (100) substrates. For transmittance measurements, optical absorption and bandgap evaluation as well as

Optical Materials EXPRESS

electrical resistivity characterization, the AZO films were deposited on double side polished glass wafers (fused silica). Characterization of the AZO films was done by four-point probe resistance measurements, atomic force microscopy (AFM), scanning electron microscopy (SEM), X-ray photoelectron spectroscopy (XPS), X-ray diffraction (XRD), and spectroscopic ellipsometry. All work was carried out in a class 100 cleanroom.

2.1 ALD growth conditions

Three temperature regimes were selected (150 °C, 200 °C and 250 °C) in order to cover most of the ZnO ALD temperature window [18,42]. AZO with various Al:ZnO ratios was deposited in a thermal, hot-wall ALD system (Picosun R200) on flat silicon (100) and fused silica substrates. Precursors were obtained from Stream Chemicals. ZnO was deposited using diethylzinc (Zn $(C_2H_5)_2$, DEZ) and deionized water (H_2O), whereas Al doping was introduced by a single cycle of trimethylaluminium ($Al(CH_3)_3$, TMA) and H_2O into the ZnO matrix made by "*n*" cycles of "DEZ+H_2O". This notation defines an AZO macrocycle used in this work: "n" cycles of "DEZ+H_2O" and 1 cycle of "TMA+ H_2O". In this case, for example, "D10" corresponds to 9 cycles of DEZ + H_2O and one cycle of TMA + H_2O. AZO films were deposited with "*n*" between 4 and 34 with 5 cycles of intermediate steps. Table 1 summarizes the parameters of one ALD macrocycle. Each precursor is introduced into the reactor chamber twice with a very short purge time of 0.5 s in-between the pulses. After this two precursor exposures, the very long purge time of 20 s follows. Such an approach is suitable for passivation of very high aspect ratio structures where it is necessary to make sure that the precursor molecules diffuse and react with a complicated surface topology such as deep holes, trenches or pillars. Prolonged purge times secure that the excess precursor and the reaction by-product are not residing on a sample.

Table 1. Recipe for one AZO macrocycle.

Precursor	Number of repetitions	Carrier gas (N_2) flow (sccm)	Pulse time (s)	N_2 Purge (s)
DEZ		150	0.1	0.5
DEZ		150	0.1	20
H_2O	4-34 (D5-D35)	200	0.1	0.5
H_2O		200	0.1	20
TMA		150	0.1	0.5
TMA		150	0.1	20
H_2O	1	200	0.1	0.5
H_2O		200	0.1	20

The overall numbers of deposited macrocycles were chosen for certain temperatures so that the overall thickness of the deposited AZO layers is as close to 100 nm as possible. The thickness was measured by spectroscopic ellipsometry. A summary of the deposition conditions and the scheme of ALD of AZO layers are shown in Fig. 1.

Optical Materials EXPRESS

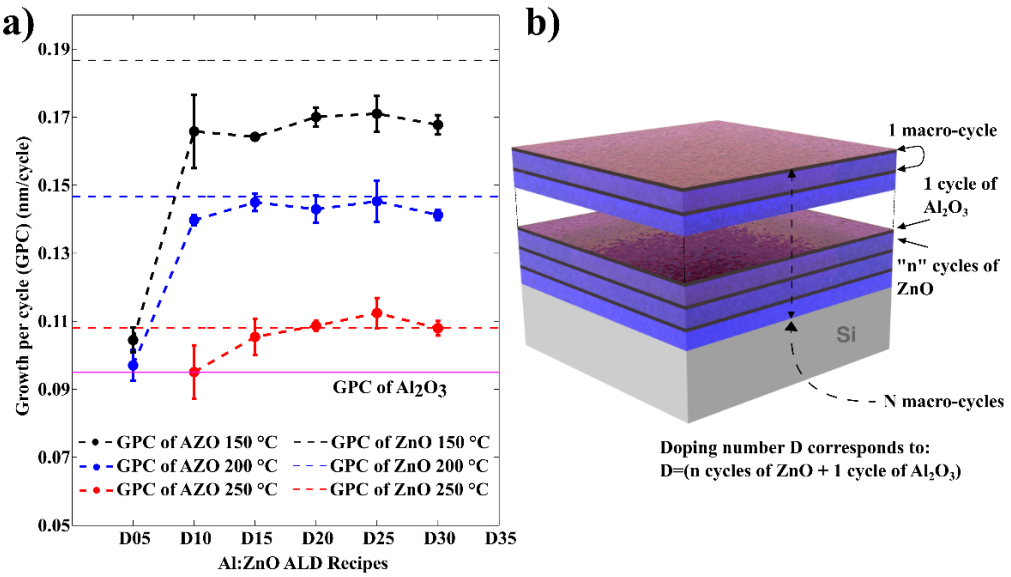

Fig. 1. ALD deposition conditions. a) Growth per cycle of Al_2O_3 ZnO and AZO for each temperature regime: 150 °C, 200 °C and 250 °C. b) Schematic drawing of deposited AZO layers and concept illustration of doping "D" number.

The deposition rate of undoped ZnO was measured to be 0.18 nm/cycle, 0.15 nm/cycle and 0.11 nm/cycle for temperatures of 150 °C, 200 °C and 250 °C respectively. The corresponding deposition rate of Al_2O_3 is 0.09 nm/cycle with negligible deviations with temperature (see Fig. 1(a)). These values are in agreement with the previously reported results [42]. The thickness of an AZO film can be calculated using the following expression: $T = N \cdot (n \cdot GPC_{ZnO} + GPC_{Al2O3})$. Here, T is the measured thickness, N is the total number of deposited macrocycles and n is the number of DEZ + H_2O cycles within one macrocycle. GPC_{ZnO} and GPC_{Al2O3} are the deposition rates (growth-per-cycle) of ZnO and Al_2O_3, respectively. In many practical cases, however, the deposition rate of Al_2O_3 can be assumed identical to the deposition rate of ZnO. In such scenario, the film thickness becomes $T = N \cdot D \cdot GPC_{AZO}$ where $D = n + 1$ according to the concept presented in Fig. 1(b). This assumption is valid in the temperature region 200-250 °C, but in the case of 150 °C the difference in the growth rates between ZnO and Al_2O_3 becomes significant and the GPC ratio of these oxides should be treated separately.

The more important discrepancy in deposition rate occurs when the thickness of the ZnO host becomes small as in the case of the D05 recipe for depositions with 150 °C and 200 °C, and D10 with 250 °C (Fig. 1(a)). The difference here is so pronounced that it cannot be explained by a slower deposition rate of Al_2O_3. Several explanations have been proposed for the reason of this behavior. It could be related to hindering of the ZnO phase after TMA/H_2O pulses [8] or the etching of ZnO by TMA [9]. Next section will reveal that this high Al-doped AZO films indeed contains more amorphous dielectric Al_2O_3 rather than ZnO.

2.2 ALD Elemental analysis

X-ray Photoelectron Spectroscopy (XPS) chemical trace analysis (performed using an XPS system from Thermo Scientific equipped with monochromatic Al Kα X-rays) revealed a high-quality chemical film with no observable impurities. Figure 2(a) shows a scan of an AZO D25 250 °C sample. Prior to XPS measurements, the film surface was sputtered in situ with Ar^+ ions in order to get rid of native airborne hydrocarbons. Thermo Avantage v5.948 software was used in order to calculate the Al concentration in the AZO films. Figure 2(b) shows a high-resolution Al2p area for ZnO/AZO deposited at 250 °C. The obtained aluminum

Optical Materials EXPRESS

concentrations are plotted for the ALD recipes in Fig. 2(c). Remarkably, the actual concentration of Al is significantly higher than the one predicted by simple estimation. With ideal ALD behavior, the Al concentration can be calculated using the simple expression: $Al(\%) = 100\% \cdot GPC_{Al2O3} / (GPC_{Al2O3} + n \cdot GPC_{ZnO})$. The straight dashed blue line in Fig. 2(d) shows the ideal case, while XPS measured Al concentrations are higher. These observations is confirmed by other experimental techniques such as energy dispersive X-ray spectroscopy (EDX) [5] and X-ray fluorescence (XRF) [8]. The proposed explanation is the inhibition of ZnO growth after the TMA + H_2O cycle. An alternative explanation suggests that TMA exposure etches the underlying ZnO, causing the mass loss [9].

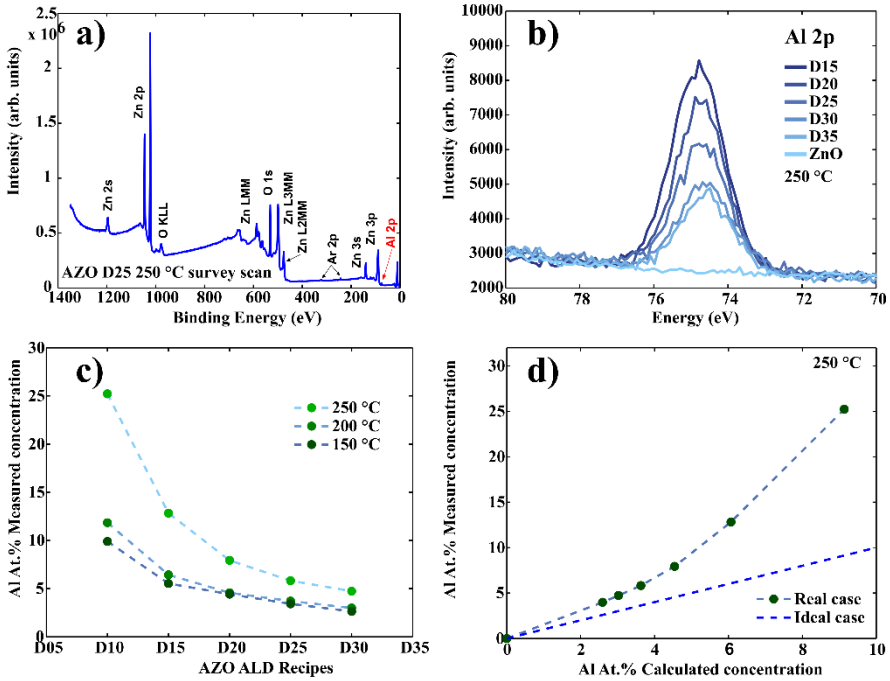

Fig. 2. XPS investigation of AZO layers. a) The typical survey scan of AZO/ZnO. b) High-resolution scan for Al2p region for AZO/ZnO samples prepared at 250 °C. c) Measured Al concentration in AZO films prepared at three temperatures: 150 °C, 200 °C and 250 °C. d) Deviation of the measured Al at. % concentration from the theoretical estimation in case of 250 °C deposition temperature.

2.3 Morphology of deposited AZO layers

Surface morphology of deposited 100 nm ZnO/AZO thin films was analyzed by scanning electron microscopy (FE-SEM Supra 60VP from Zeiss) and atomic force microscopy (AFM, Icon PT from Bruker). SEM images (Fig. 3(a)) reveals polycrystalline nature of deposited thin films. AFM inspections (Fig. 3(b)) of deposited ZnO/AZO films D10-D35 at 250 °C reveal a surface roughness of approximately 2 nm RMS, which slightly decreases with increasing the Al content in the films. In the case of D10, the Al_2O_3 phase dominates what results in a roughness below the acceptable detection value. The AZO films deposited at 250 °C tend to obtain a cylindrical morphology, which can be related to preferred (002) ZnO crystal orientation growth. Discussion follows in the next section.

Optical Materials EXPRESS

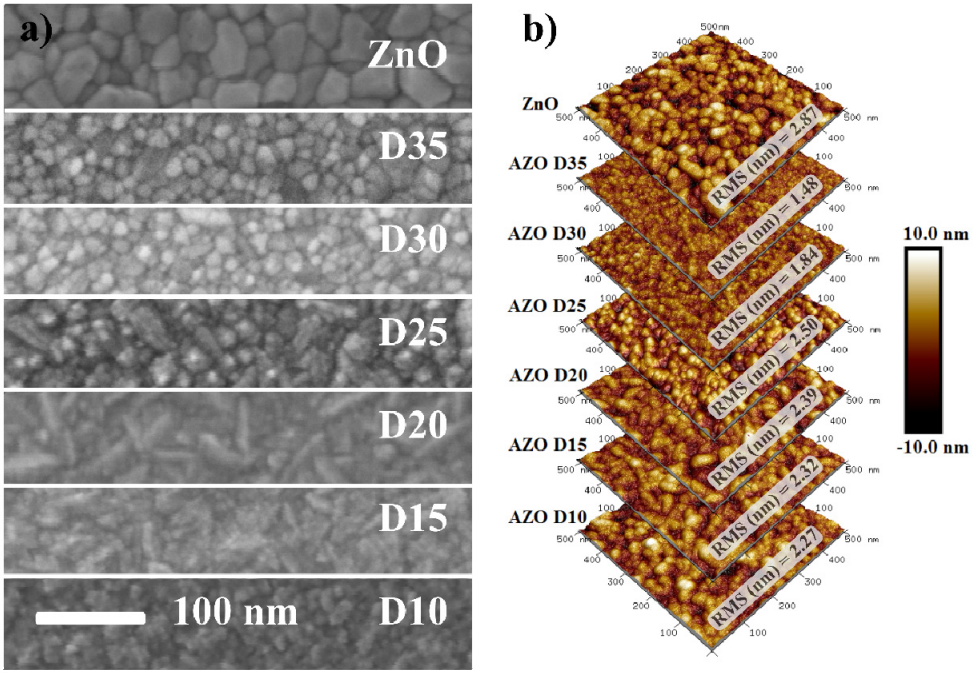

Fig. 3. Morphology inspection. a) SEM and b) AFM images (500 nm × 500 nm) of flat AZO samples prepared at 250 °C.

2.4 XRD measurements

The crystal orientations were studied by analyzing X-ray diffraction (XRD) patterns obtained with a Bruker D8 diffractometer equipped with a Göbbel mirror. θ - 2θ scans were acquired in Bragg-Brentano geometry with a Cu Kα X-ray source. The instrumental broadening was taken into account by performing a LaB_6 powder standard scan. The obtained scans were additionally checked for the alignment by controlling the corresponding position of the Si(400) $K\alpha_1$ and Kβ peaks originating from the substrates.

XRD results are summarized in Fig. 4. They revealed that the AZO films deposited at 250 °C are polycrystalline with preferential (002) orientation. Two main peaks were found: (002) and weak (101), all other orientations were not observed in the 2θ range between 20° and 72°. Figure 4(a) shows ZnO/AZO XRD patterns at 250 °C.

At 150 °C growth temperatures (100) orientation was favored. Increase in the deposition temperature to 200 °C results in appearance of both (100) and (002) peaks. Finally, AZO films deposited at 250°C were strongly (002) orientated with minor (101) components (Fig. 4(a)), while (100) orientation vanishes. The noisy part from quasi-forbidden Si(200) reflections [43] was removed from the scans.

The orientation peaks move to higher 2θ values with increasing Al concentrations in the films. When the concentration becomes too high (as in the case of the D15 and D10 recipes) films become amorphous (Fig. 4(a)). Characterization of the crystal structure was conducted by fitting the Lorentzian functions through the (002) and (101) peaks (Fig. 4(b)). According to the Bragg law:

$$n\lambda = 2d\sin\theta \tag{1}$$

The d interplanar spacing of the ZnO Wurtzite crystal structure is related to lattice parameters a and c by:

Optical Materials EXPRESS

$$\frac{1}{d^2} = \frac{4}{3}\left(\frac{h^2 + hk + k^2}{a^2}\right) + \frac{l^2}{c^2}, \tag{2}$$

where h, k and l are the Miller indices.

In this case, the (002) and (101) peaks were used to calculate lattice parameters. Figure 4(c) shows that the a parameter does not undergo any significant changes, while constant c reduces from 5.20 Å (undoped ZnO) to 5.12 Å (D20) in an almost linear trend. Compression of the lattice constant c is due to replacement of larger Zn^{2+} ions by smaller Al^{3+} (ionic radii, 72 and 53 pm respectively).

The Lorentzian fit through the measured peaks allows estimation of corresponding grains sizes. The method is based on the Scherrer equation using either the full width at half maximum (FWHM) or integral breadth (area below the peak normalized by its height):

$$D = \frac{K\lambda}{\beta_{INT}\cos\theta}, \text{ where}$$
$$\beta_{INT} = \beta_{observed\,INT} - \beta_{istrumental\,INT}. \tag{3}$$

Here, K is the Scherrer factor, λ is the wavelength of Cu $K\alpha_1$ radiation, θ is the Bragg angle and β_{INT} is the instrument corrected integral breadth, where $\beta_{observedINT}$ and $\beta_{instrumentalINT}$ are the corresponding integral breadth broadenings of an observed peak and instrumental correction, respectively. The use of the integral breadth leads to a more accurate estimation of the grains size compared to the FWHM approach since it takes the Lorentzian tails of diffraction peak into account [44]. However, additional factors responsible for peak broadening, such as microstrains, requires more rigorous deconvolution analysis with the implementation of Pseudo-Voigt functions, which are weighted superpositions of Gaussian and Lorentzian contributions [44]. This goes above the scope of this research since it requires a more intense X-ray source and better-accrued statistics.

Estimated grain sizes are presented in Fig. 4(d) for all of the investigated temperatures. The grains with (002) orientations are 2-3 times smaller than the corresponding (100) oriented grains. It seems that for AZO films the (002) grains become larger with increasing of the Al concentration, until approximately 4 at. % of Al, and then the grains size decreases. The (101) oriented crystallites size was not calculated due to bigger uncertainties (smaller and noisier peaks in XRD spectrum).

Optical Materials EXPRESS

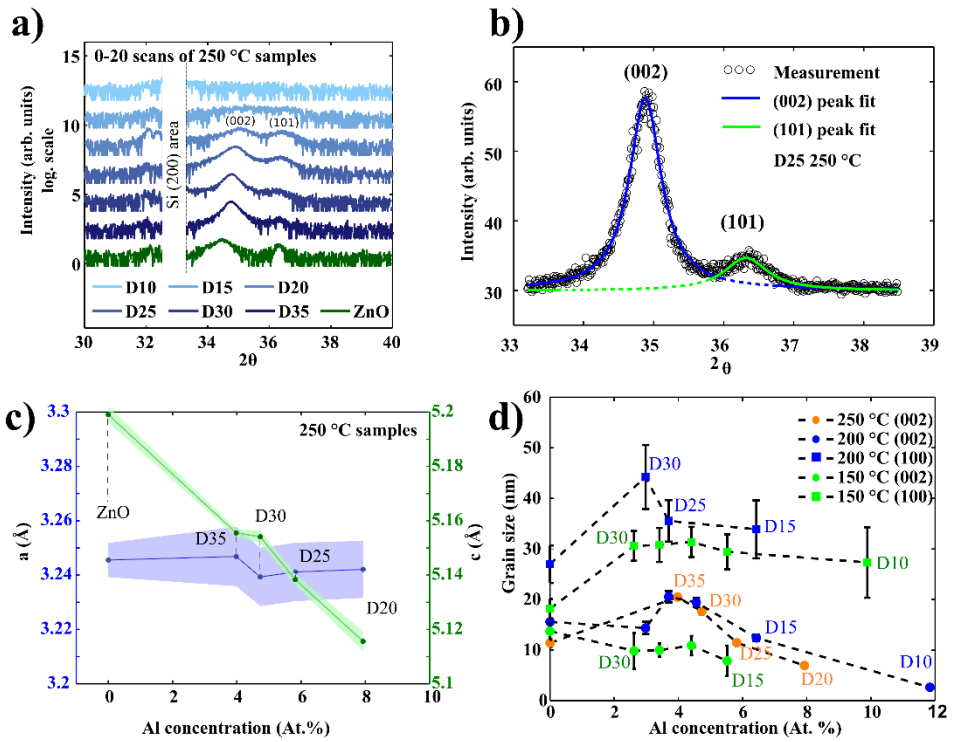

Fig. 4. XRD analysis. a) Diffraction patterns of all AZO/ZnO samples prepared at 250°C shown in logarithmic scale. b) Typical area around (002) and (101) ZnO crystal orientations with applied Lorentzian fit function. c) ZnO lattice dimensions constants *a* and *c* as a function of Al at. % concentration (samples deposited at 250 °C). d) Estimated grains size as a function of Al concentration in the samples (samples corresponding to all three deposition temperatures 150°C, 200°C and 250°C).

2.5 Electrical properties

A conventional four-point probe (Veeco FPP-5000) was used for resistivity measurements. Strong correlation between the resistivity, Al concentration, and grains sizes was found (see Fig. 5). Undoped ZnO 100 nm films have a resistivity of 8 mOhm·cm except ZnO grown at 250 °C. The high resistivity of this particular film is attributed to small pores in the film. The small pores around bigger ZnO clusters are visible in the SEM image in Fig. 3(a).

For 100 nm thick AZO films the lowest resistivity of 1.3-1.4 mOhm·cm is achieved at the Al level around 4 at. %. In general, the resistivity of 150 °C prepared films is higher compared to 200 °C and 250 °C (see Fig. 5(a)). Figure 5(b) shows the dependencies between the (002) and (100) grains size and resistivity. The general trend is that the larger the grains, the lower the resistivity. This is observed for both orientations, regardless of the growth temperature. Several reports [5,6,9], suggest that the resistivity of AZO films strongly correlates with the degree of the pronunciation of the (002) orientation. This work does not provide a direct prove of this concept. Indeed, the AZO films were grown at 250 °C and without visible (100) orientation have the strong tendency of the resistivity reduction with an increase of (002) grains (Fig. 5(b)). However, this tendency is common in all of the grown films with both orientations.

Optical Materials EXPRESS

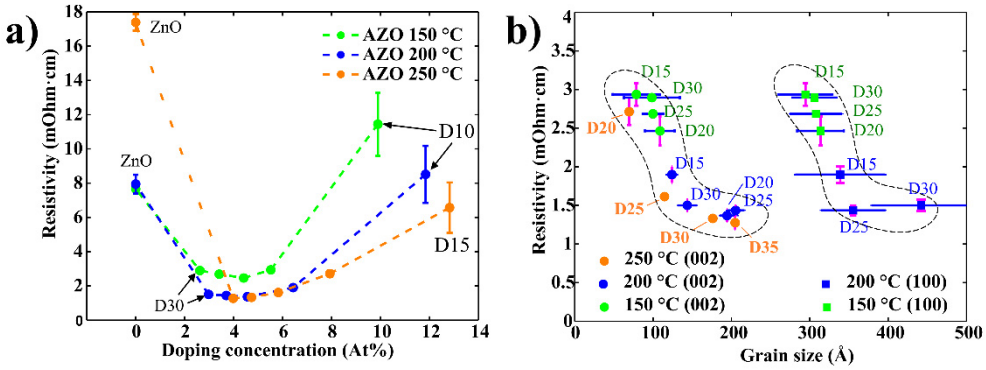

Fig. 5. The resistivity of all of the prepared AZO/ZnO samples as a) function of Al at. % concentration and b) resistivity vs. grains size for AZO samples.

2.6 Optical properties

The optical characterization of the AZO films was conducted using spectroscopic ellipsometry (Ellipsometer VASE from J.A. Woolam Co.). Figure 6 illustrates results for 100 nm AZO films grown at 250 °C. In spectroscopic ellipsometry, the parameters of amplitude component Ψ and phase difference Δ were measured over a certain wavelength range (in this case 210 – 1690 nm), where Ψ and Δ are defined by:

$$\frac{r_p}{r_s} = \tan(\Psi)\cdot e^{i\Delta}, \tag{4}$$

where r_p and r_s are the reflection coefficients of p and s polarized light. The experimentally obtained values of Ψ and Δ were fitted using the Kramers-Kronig relations to obtain permittivity values. Figure 6(a) illustrates the real and imaginary parts of the permittivity for ZnO and AZO films. It shows that the permittivity of AZO decreases rapidly with increasing the wavelength, while the permittivity of ZnO remains almost constant. Such results have been very recently discussed [45,46] in the context of plasmonic applications of AZO films close to the epsilon-near-zero (ENZ) point. The wavelength of this zero-crossing corresponds to plasma frequency ω_p. Observation of the negative permittivity of the AZO films is above the ellipsometer wavelength range, but extrapolation of the Kramers-Kronig functions can predict ω_p values, with the highest value of 166.44 THz (1800 nm) correspondent to a D25 AZO film deposited at 250 °C. Screened plasma frequencies are shown in Table 2. The coatings deposited at 150-200 °C temperatures have sufficiently lower ω_p (not shown here).

Figure 6(b) displays the transmission spectra for 100 nm AZO films grown at 250 °C on fused silica. In this experiment, the ellipsometer was used in the transmission mode, where the moving arms of the source and detector were placed at 90° to the surface normal. In the visible range, all of the films exhibit an average optical transmittance greater than 90%. The spectrum shows a sharp absorption edge in the ultraviolet range, which shifts toward the shorter wavelengths (blue shift), as the concentration of Al in AZO samples increases. The absorption edge can be used to estimate an optical band gap of AZO thin films. Since ZnO is direct band semiconductor, it can reasonably be assumed that absorption coefficient α and the Tauc relationship [47] are given by:

$$\alpha \propto -\ln(T) \tag{5}$$

$$(\alpha h\nu)^2 \propto (h\nu - E_g). \tag{6}$$

Optical Materials EXPRESS

These relations are plotted in Fig. 6(c) and 6(d). The energy band gap (E_g) can be obtained by plotting $(\alpha hv)^2$ vs hv and linearly extrapolating the fit of the linear region to $\alpha = 0$ as shown in Fig. 6(e). As depicted in Fig. 6(e), the higher the Al concentration in the film, the higher the optical bandgap is. It can be explained by the increase of the carrier concentration which is caused by Al-doping. This widening of the optical band gaps is generally attributed to the Burstein-Moss shift effect [48,49].

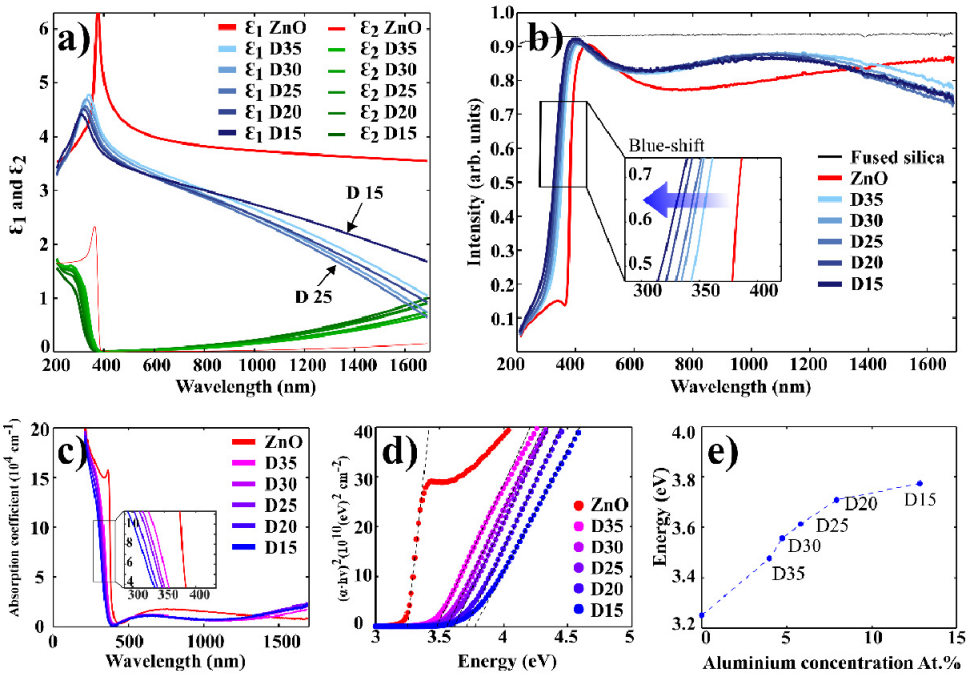

Fig. 6. Optical properties of the AZO/ZnO thin films prepared at 250 °C. a) Real ε_1 and imaginary ε_2 parts of permittivity. b) Transmission spectra with a small absorption edge shift (shown in the inset). c) Absorption coefficient. d) The plot of $(\alpha hv)^2$ versus photon energy (Tauc plot). e) Optical bandgap as a function of Al concentration.

Table 2. Screened plasma frequencies from 250 °C AZO thin films retrieved from extrapolated ε1(λ) functions.

ALD Recipe	ZnO	D15	D20	D25	D30	D35
ω_p (THz)	-	123.71	151.43	166.44	158.14	149.70

3. Fabrication of AZO high aspect ratio pillars and tubes

Analysis of 100 nm AZO thin films reveals that AZO deposited at 250 °C has the lowest resistivity, highly preferential growth along the *c* axis with (002) crystal orientation and the most pronounced decrease in the permittivity with increasing the wavelength, compared to the films deposited at lower temperatures. It makes these films excellent candidates for plasmonic components in optical metamaterial structures. Among them, D25 AZO has the highest ω_p. This recipe is selected for fabrication of AZO HMM, based on free-standing pillars. According to theory [31], such metamaterial structures might possess hyperbolic dispersion of type I in the mid-IR optical range.

Double side polished (DSP), 150 mm (100) Si wafers were selected for device fabrication. They were RCA cleaned and later oxidized in a conventional quartz tube (furnace from Tempress) using a dry oxidation process based on O_2 at 1100 °C, resulting in a 200 nm SiO_2

Optical Materials EXPRESS

layer on Si. Next, a 2 μm amorphous Si layer was deposited on the SiO_2 surface using a conventional low-pressure chemical vapor deposition (LPCVD) process (furnace from Tempress) based on SiH_4 at 560 °C. This procedure enables the preparation of home-made silicon-on-insulator (SOI) substrates.

The main steps in the fabrication of pillars and tubes are shown in Fig. 7. Initially, silicon holes were etched in SOI wafers by deep-UV lithography and DRIE (Fig. 7(a)-7(c)). The holes were arranged in a square lattice with the pitch of 400 nm. The template was then filled with an ALD D25 AZO coating (Fig. 7(d)) at 250 °C. The thickness of the deposited AZO depends on the desired output. An entire filling would result in the formation of pillars, while partial deposition leads to fabrication of hollow tubes. After removal of the top parts by Ar^+ ion sputtering (Fig. 7(e)), the silicon core between the ALD coated holes was etched away during the last step. Figure 7(f) represents the final structures. Each process step was carefully analyzed using cross-sectional SEM imaging.

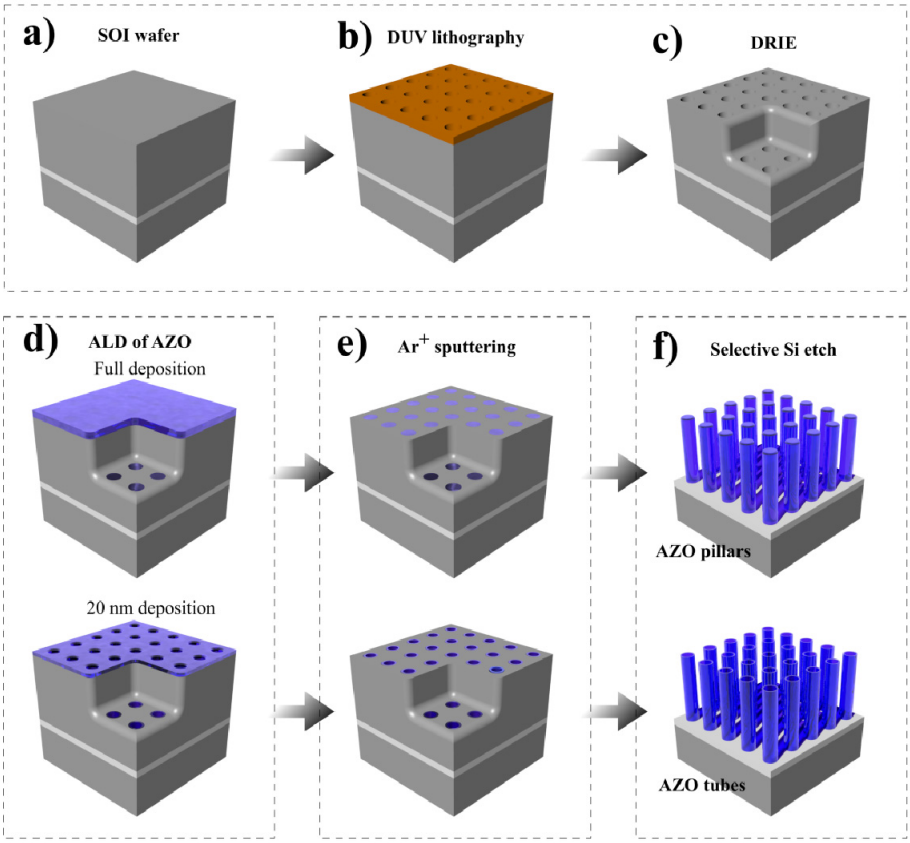

Fig. 7. Schematics of the fabrication flow. a) Home-made SOI substrates. b) Deep-UV lithography. Resist spin coating, baking, exposure and developing. c) DRIE etching, fabrication of initial Si template. d) ALD deposition of D25 AZO at 250 °C. Partial deposition will lead to fabrication of tubes, while complete filling will create full pillars. e) Removal of the top AZO layer by Ar^+ sputtering. f) Silicon host removal using conventional RIE process.

3.1 Template preparation

Conventional deep-UV lithography (DUV stepper: Canon FPA-3000 EX4) was implemented for defining the hole patterns (dots in a square lattice, with a pitch of 400 nm) on 1 × 1 cm^2 scale chips. The normal procedure includes a bottom antireflective coating (BARC) and photoresist coating, followed by spray development. To promote adhesion and minimize

Optical Materials EXPRESS

interference effects, the substrate surface was coated with a 65 nm thick BARC coating (DUV42S-6, Brewer Science, USA) followed by a bake-out at 175 °C for 60 s. A positive photoresist (KRF M230Y, JSR Micro, NV), was spin-coated to a thickness of 360 nm, baked at 130 °C for 90 s and exposed (exposure dose of 840 J/m2) on a patch with sizes of 1 × 1 cm^2. Thereafter, DRIE was used to fabricate holes in the silicon with a depth of 2 μm.

3.2 DRIE etching

DRIE etching (DRIE Pegasus from SPTS) was performed in a switched Bosch process consisting of cyclic steps of etching and passivation. The processing temperature was kept at 0 °C and the process pressure at 10 mTorr. Three main steps were used for the Si template fabrication: etching of the BARC layer, high anisotropic silicon etching (Table 3 summarizes the Bosch process parameters) and resist removal. The BARC etch proceeds for 45 s using 40 sccm O_2 plasma with coil and platen powers of 400 W and 20 W, respectively. The depth of holes was controlled by adjusting the number of cycles (85 cycles correspond to 2 μm deep holes). The strict control of the etching depth is required on bare Si substrates though it is less important for SOI wafers with a SiO_2 stop layer. The last step in Si holes fabrication is the removal of the remaining resist, which was done using O_2 plasma for 2 min with an O_2 flow of 100 sccm. The coil and platen powers were 800 W and 20 W, respectively. The shape of the produced Si-holes template structures was carefully investigated by SEM in the cross-sectional mode by sacrificing some of the prepared structures. The achieved diameter of the holes is slightly larger than 200 nm due to imperfections in the etching process, especially in the middle part of the cylinders. Prior to the next step (ALD deposition), the prepared template structure received additional O_2/N_2 plasma treatment in order to remove any possible organic residuals from resist coatings and surroundings.

Table 3. DRIE parameters for Si template fabrication.

	Gasses	Passivation (1.5 s)	Etching (2.75 s)
Process gas flow (sccm)	C_4F_8	50	20
	SF_6		60
	O_2		5
Powers (W)	Coil	600	400
	Platen		40

3.3 ALD deposition

An AZO film has been deposited with the D25 recipe on a DRIE prepared Si template with holes at the temperature of 250 °C. Two ALD depositions with two thicknesses were made. The first one which allows the full pillars fabrication required deposition of a 100 nm D25 AZO film in order to fill the holes entirely. The second run was a deposition of only a 20 nm AZO D25 thin film in order to test and verify technology. This allows fabrication of thin, free-standing AZO cylinders. SEM cross-sectional inspections reveal homogenous and conformal coatings. Due to minor imperfections in Si etching processes, a small empty gap (with a radius about 25 nm) in the middle of the structures is created after ALD filling in the case of full pillars. The thickness of the ALD coating in full pillars case is around 100 nm, which with the empty gap in the center of the structures results in the pillars with approximately 250 nm diameter.

3.4 Ar^+ ion etching of deposited AZO and selective removal of the Si host

Pure physical Ar^+ ion sputtering (Ionfab 300 plus from Oxford Instruments) was implemented for removal of the deposited AZO top layer in order to get an access to the silicon core as illustrated in Fig. 7(e). Here the process was tuned to the etch rate of 20 nm/min which provided well-controlled top layer breakthrough.

Optical Materials EXPRESS

Removal of the silicon host is the last step in fabrication. Selective silicon etching (template removal) proceeded using continuous isotropic etch in a conventional reactive ion etching tool (RIE, from SPTS) based on a continuous SF_6 process at the substrate temperature of 20 °C. The SF_6 gas flow was kept constant at 35 sccm and the process pressure and coil power were 80 mTorr and 30 W, respectively. This process proceeds with extreme selectivity towards the deposited AZO layer without any observable harm brought on the AZO pillar structure. The proof of selectivity is demonstrated in the case of 20 nm thin AZO tubes. No imperfections or corrugations on the tubes were observed even though the ratio of thickness to height was extreme: 1:100 (20 nm to 2μm). Detailed electron microscopy characterization follows in the next section.

4. Structures characterization

The fabricated AZO D25 pillars were carefully investigated using SEM and transmission electron microscopy (TEM) characterizations. The tubes are thin enough to be electron transparent. This allows estimation of the grains size and comparison with the XRD measured values. It should be mentioned, that the grains sizes are expected to be dependent on the thickness of the deposited AZO layer. In this work, no other thicknesses than 100 nm were XRD investigated. However, it is expected that physical and optical properties of AZO are correlated with the layer thickness [12].

4.1 SEM images

Figure 8 shows the fabricated structures standing on a 200 nm thick SiO_2 layer (Fig. 8(a) and 8(b) for pillars and tubes respectively). The samples were tilted by 30° inside the SEM chamber and the corner of each sample was visualized using a variable pressure secondary electron (VPSE) detector at 15 kV with a bias voltage of + 350 V and N_2 pressure of 20 Pa. The high magnification inset images of Fig. 8 were taken using an in-lens detector at 10 kV. Here the individual pillars/tubes shape is clearly seen.

4.2 TEM characterization

The crystallographic profile and microstructural analysis of D25 AZO tubes were studied using TEM (monochromatic FEI Titan TEM). The experiment was conducted at 300 kV with a Cs image corrector (CETCOR unit from CEOS). The elemental mapping using energy-dispersive X-ray spectroscopy (EDX) was performed on selected AZO pillars using a probe-corrected electron microscope (FEI Titan 80-200 ChemiSTEM) equipped with four symmetric SDD detectors.

Figure 9 shows TEM results for pillars and tubes. A magnified image of the pillar top part is depicted in Fig. 9(a). The selected area electron diffraction (SAED) reveals crystallographic information. Figure 9(b) shows the diffraction pattern which tells that the produced AZO film is polycrystalline with (002), (100) and (101) strongest orientations. Other minor ZnO orientations were observed too. The traces corresponding to (102), (110), (103), (112) *etc.* orientations were below the detection sensitivity of the XRD equipment.

Dark-field TEM images (Fig. 9(c) and 9(d)) of the AZO tubes reveal the information of the crystal grains size. The full AZO pillars are too thick for transparency measurements, while 20 nm thin tubes are sufficiently thin for such purposes. The crystalline grains visible in Fig. 9(c) and 9(d) have dimensions of approximately 10 nm, which correlates well with the size obtained by XRD. However, the AZO grains measured and depicted in Fig. 4 comes from 100 nm thick films and cannot be directly compared with the crystalline structure of the AZO tubes. Figure 9(e) depicts a high angle annular dark-field (HAADF) imaging of an AZO pillar and EDX elemental mapping proving that ZnO was indeed doped homogeneously.

Optical Materials EXPRESS

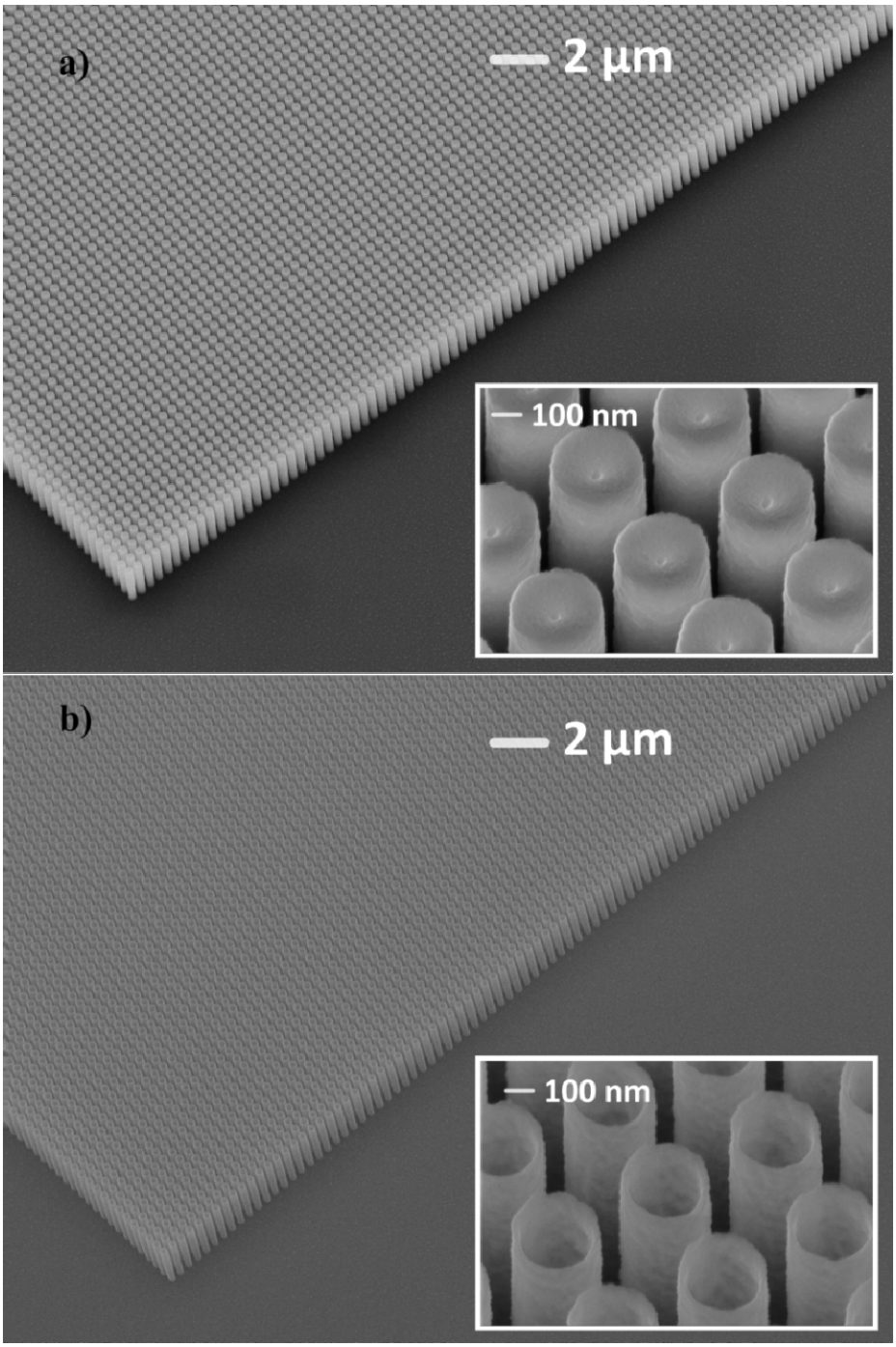

Fig. 8. Bird-eye-view SEM images of the prepared structures: a) AZO pillars and b) AZO tubes. The insets show an enlarged view of the metamaterials.

Optical Materials EXPRESS

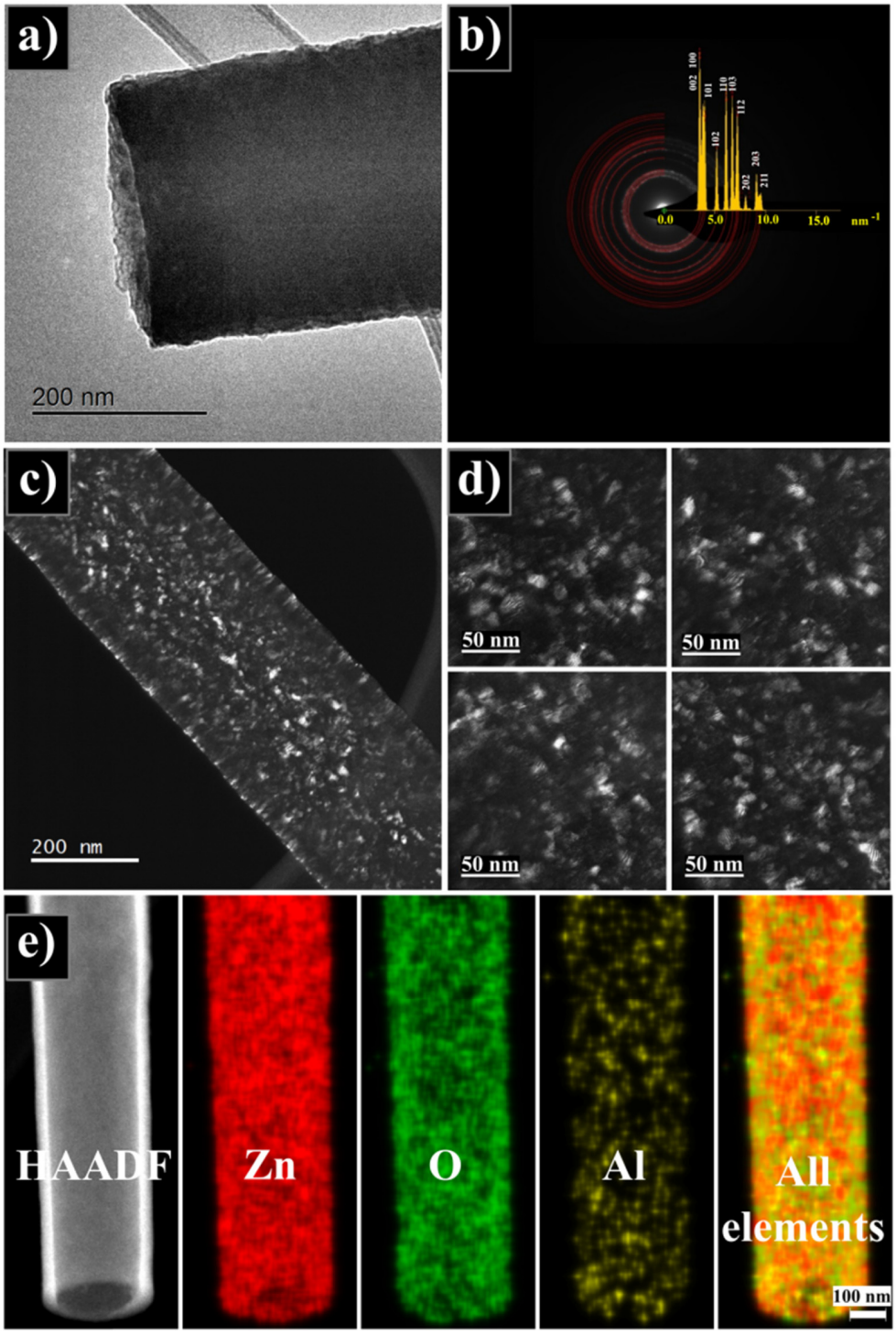

Fig. 9. TEM inspection. a) High-resolution TEM image of the produced pillars. b) SAED pattern of AZO D25 pillar. c) and d) are dark field images: c) is the image at low magnification, d) are enlarge images of the same area with different positions of the object aperture. e) EDX elemental mapping and HAADF imaging of AZO nanopillar.

Optical Materials EXPRESS

5. AZO pillars FTIR characterization

In order to test the performance of the arrays of free-standing pillars as a metamaterial, AZO pillars were grown directly on DSP Si wafers without any SiO_2 stop-layer at the bottom. The entire fabrication procedure is as illustrated in Fig. 7 and the output was the same as previously described. Avoiding a SiO_2 stop layer excludes unnecessary complexity in optical characterization, but demands more careful fabrication conditions. The last step presented in Fig. 7(f), requires strict control of the etching depth. Otherwise, the pillars would collapse in case of the overetch.

First, the permittivities of the individual dielectric (Si) and plasmonic (AZO) components need to be established.

5.1 Dielectric functions of individual Si and AZO thin film components

In order to determine the permittivity of a 100 nm thick D25 AZO film, the permittivity of the DSP silicon wafer on top of which the AZO film was deposited needs to be found. In this regard, the reflectance spectrum of the bare DSP Si wafer was calculated using the intensity transfer matrix method [50] and measured using FTIR (VERTEX 70 FTIR spectrometer from Bruker). The calculated reflectance spectrum was then fitted to the measured one using an algorithm based on the Levenberg-Marquardt method [51], to find the permittivity of the Si substrate. Afterward, the same procedure was carried out for the AZO film on the DSP Si substrate, considering the airgap and the FTIR sample holder's aluminum mirror under the sample in calculations. The Drude-Lorentz model was used for fitting the dielectric function of the Si substrate and AZO thin film:

$$\varepsilon(\omega) = \varepsilon_\infty \left(1 - \frac{\omega_p^2}{\omega^2 + i\omega\gamma}\right) + \sum_j \frac{S_j \omega_{f,j}^2}{\omega_{f,j}^2 - \omega^2 - i\omega\Gamma_j} \tag{7}$$

The Drude term contains ε_∞, ω_p and γ, which are the high-frequency dielectric constant, plasma frequency and electrons plasma damping, respectively. The Lorentzian part of dielectric function $\varepsilon(\omega)$ is represented by the summation in Eq. (7), where S_j, ω_{fj} and Γ_j are the strength, resonance frequency and damping for the j^{th} Lorentzian oscillator, respectively. Figures 10(a) and 10(c) show the measured and the fitted reflectance spectra for the Si substrate and the AZO thin film, respectively. The dips at around 11 μm and 16.5 μm originate from the Si absorption, while the 9 μm and 13 μm dips correspond to absorption in native SiO_2 [52]. Five Lorentzian terms with ε_∞ from Eq. (7) were used in order to retrieve the permittivity of the Si substrate (fitted parameters are presented in Table 4), while only the Drude part was considered for the AZO thin film (Table 5). Retrieved permittivities are shown in Fig. 10(b) and 10(d) for Si and the AZO film, respectively.

Table 4. Retrieved dielectric function parameters for the Si substrate.

j	1	2	3	4	5
S_j	0.000389	0.000618	9.81×10^{-5}	0.000136	2.72×10^{-5}
Γ_j (THz)	3.07	1.47	1.37	2.97	0.72
ω_{fj} (THz)	15.24	18.32	22.39	26.69	33.18

Table 5. Retrieved dielectric function parameters for 100nm AZO film.

γ (THz)	ω_p (THz)	ε_∞
40.73	166.44	3.45

Optical Materials EXPRESS

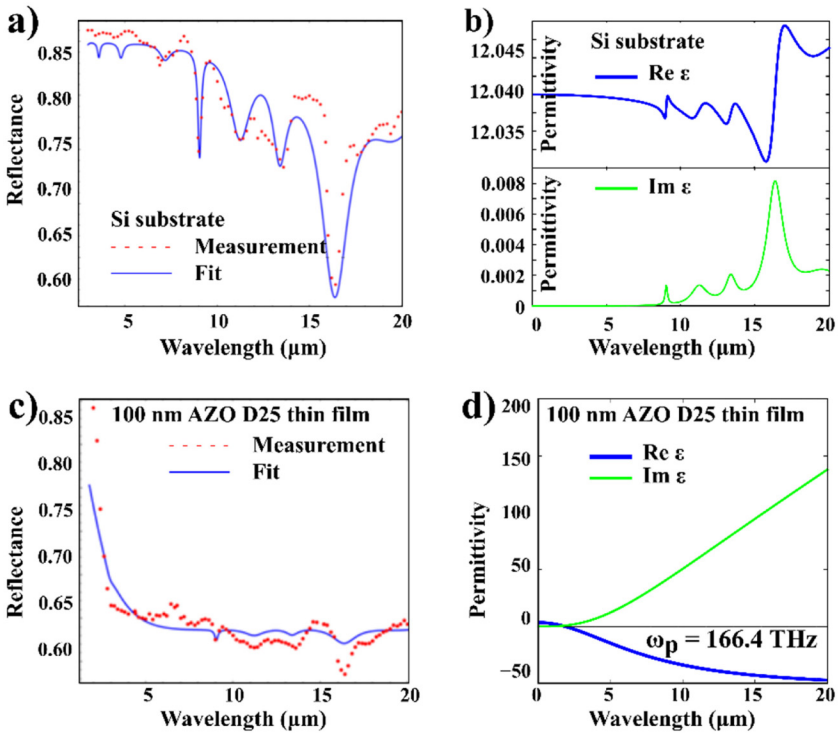

Fig. 10. a) Measured and fitted reflectance spectra for the DSP Si substrate together with b) its retrieved permittivity. c) Measured and fitted reflectance spectra for the 100 nm thick D25 AZO film together with d) its retrieved permittivity.

5.2 Dielectric functions of AZO pillars

The effective permittivities of two types of AZO pillar metamaterials, AZO pillars in air (Air/AZO) and AZO pillars in Si matrix (Si/AZO) were retrieved. Both pillar structures have the pitch of 400 nm, height of 2 μm, and diameter of AZO pillars 250 nm. The effective ordinary, ε_o, and the effective extraordinary permittivities, ε_e, correspond to the cases where the electric field is perpendicular and parallel to the pillars, respectively. The effective permittivities of the structure were retrieved from free-space FTIR reflection spectroscopy. Measurements were conducted for the wavelength range of λ = 1.428 – 20.0 μm (7000 – 500cm^{-1}). The incident light is TE-polarized (the electric field in the plane of the top surface) with the incidence angle close to the normal (12°) for measurement of the ordinary permittivity. The extraordinary permittivity was characterized by applying the TM-polarized light (the magnetic field in the plane of the top surface) with the grazing incident angle of 76°, which provides electric fields almost parallel to the pillars. The angular variation (cone divergence angle) of the input beam is $\Delta\varphi_i = \pm 1.7°$. The fitting process was carried out for the pillar metamaterials considering the Drude-Lorentz model (Eq. (7). The Drude term together with two Lorentzians was considered for ε_e of Si/AZO pillars and Air/AZO pillars. For ε_o, four Lorentzians together with ε_∞ and two Lorentzians together with ε_∞ were implemented for Si/AZO and Air/AZO pillars, respectively. Figure 11 shows the measured and fitted reflectance spectra for the pillar metamaterials with the retrieved parameters of the dielectric functions given in Table 6.

Optical Materials EXPRESS

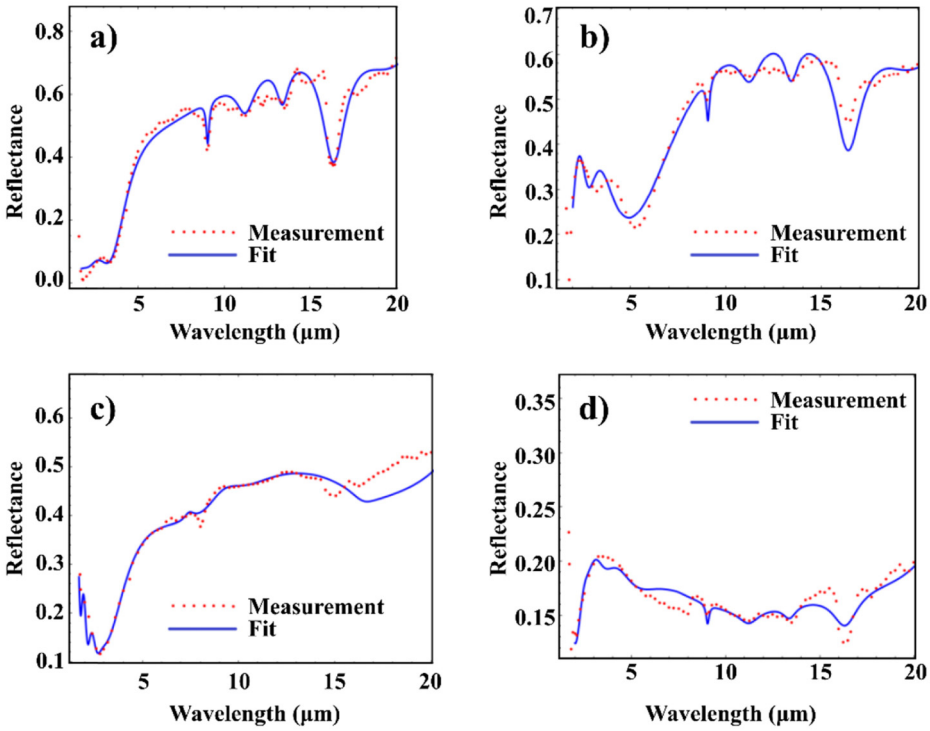

Fig. 11. Measured and fitted reflectance spectra for (a) Air/AZO ordinary, (b) Air/AZO extraordinary, (c) Si/AZO ordinary and (d) Si/AZO extraordinary cases.

Table 6. Retrieved dielectric function parameters for Air/AZO and Si/AZO pillar metamaterials. (units for plasma frequencies, damping and Lorentzian resonance frequencies are all in THz)

	S_1	S_2	S_3	S_4	Γ_1	Γ_2	Γ_3	Γ_4	$\omega_{f,1}$	$\omega_{f,2}$	$\omega_{f,3}$	$\omega_{f,4}$	γ	ω_p	ε_∞
Si/AZO: ε_o	9.35	0.10	1.43	3.87	56.37	3.48	8.32	11.02	54.63	40.32	32.19	25.51	-	-	6.16
Si/AZO: ε_e	0.16	4.31	-	-	61.72	1.19	-	-	151.01	11.48	-	-	134.78	35.22	10.47
Air/AZO: ε_o	0.98	7.48	-	-	202.50	787.76	-	-	193.65	17.97	-	-	-	-	1.29
Air/AZO: ε_e	0.40	0.12	-	-	45.97	110.42	-	-	65.22	161.82	-	-	34.40	10.83	3.46

Figure 12 shows the real and imaginary parts of the retrieved ordinary and extraordinary permittivities for both structures, as well as the calculated effective permittivities based on the effective medium approximation (EMA) theory [31]:

$$\varepsilon_o^{EMA} = \frac{(1+f)\varepsilon_m\varepsilon_d + (1-f)\varepsilon_d^2}{(1+f)\varepsilon_d + (1-f)\varepsilon_m} \tag{8}$$

$$\varepsilon_e^{EMA} = f\varepsilon_m + (1-f)\varepsilon_d \tag{9}$$

Here, f, ε_m, and ε_d are the volume fraction of the AZO pillars, the permittivity of the AZO 100 nm film, and the permittivity of the air or Si dielectric matrix components. Figures 12(a) and 12(c) show that the real and imaginary parts of the ordinary permittivity for the Air/AZO pillar structure have good agreement between the experimental and ones calculated with the EMA. Those for the Si/AZO pillar structure ordinary permittivities (Fig. 12(b) and 12(d)) exhibit moderate relevance. However, the retrieved extraordinary dielectric functions are completely different from those from the EMA predictions. According to Eq. (9) and (10), both structures should exhibit the Type-I hyperbolic ($\varepsilon_o^{EMA} > 0$, $\varepsilon_e^{EMA} < 0$) behaviour. On the contrary, retrieved extraordinary permittivities of both structures are positive in the whole

Optical Materials EXPRESS

measured wavelength range (the blue dashed lines in Fig. 12(a) and 12(b) represent the experimentally observed extraordinary case). This astonishing discrepancy implies that AZO, once being confined in the nanopillar dimensions, becomes poor plasmonic material, and its permittivity significantly deviated from that of the flat film. Typically, the ALD grown AZO films permittivity strongly depends on its thickness due to the variations in the carrier concentration [12] and an AZO film becomes less plasmonic as the thickness becomes thinner [53]. In the same analogy, the AZO pillars permittivity may also be strongly dependent on its dimensions and/or shape. A similar influence of the shape on its optical properties was reported for titanium nitride (TiN), when it takes the gyroidal form [54]. Nevertheless, the fabricated AZO metamaterial shows the pronounced anisotropy, larger than any made of dielectric components [55].

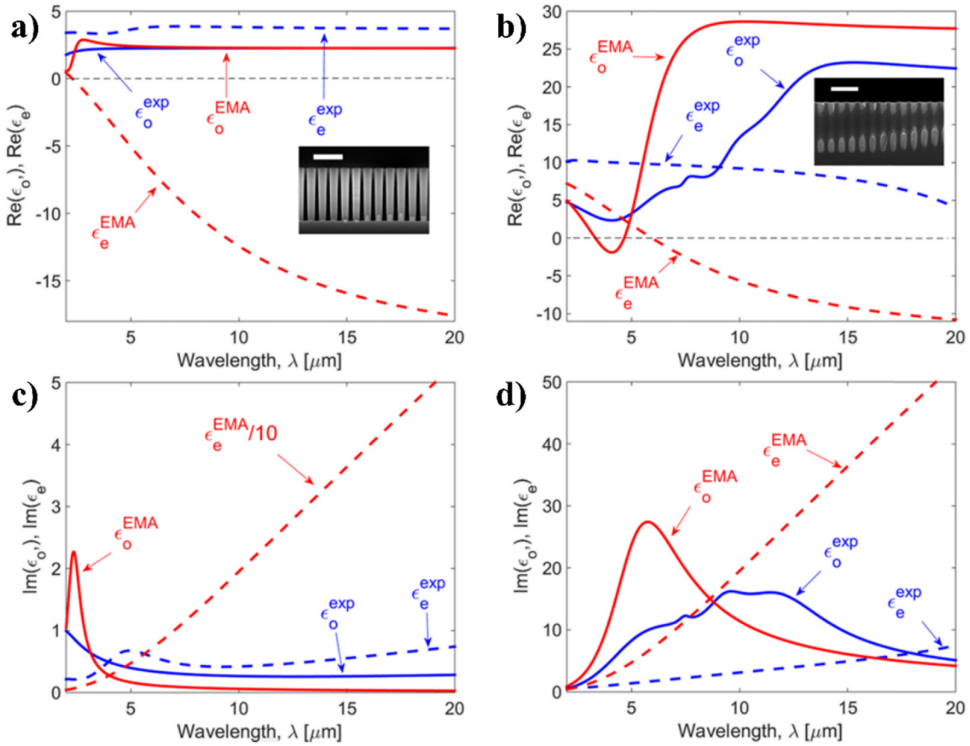

Fig. 12. Fitted real and imaginary part of effective ordinary (solid line) and extraordinary (dashed line) permittivities, ε_o and ε_e, for (a,c) Air/AZO and (b,d) Si/AZO structures, as well as effective permittivities calculated by effective medium approximation. The inset is the scanning electron microscope image of the measured Air/AZO and Si/AZO structures, respectively. The scale bars in both insets are 1 μm.

6. Summary and conclusions

In summary, highly ordered AZO pillar structures were fabricated by means of ALD, DRIE and deep-UV lithography. The fabricated structures comprise AZO nanopillars with the diameter of 250 nm and height of 2 μm. Pillars are arranged in a square lattice with a pitch of 400 nm. The whole sample has dimensions of 1 × 1 cm^2. These structural parameters can be readily adjusted by the mask used for deep-UV lithography and the subsequent process, providing more regularity in structures compared with those made by other fabrication methods [56]. The fabricated metamaterials exhibit optical properties quite different from what the effective medium theory predicts in the mid-IR optical range. Implemented technology is very flexible and robust for the realization of similar high aspect ratio

Optical Materials EXPRESS

nanostructures as it was demonstrated by fabricating 20 nm thin tubes. Plasmonic nature of AZO is strongly related to physical and optical properties of thin films and depends on deposition temperature and Al doping level. Furthermore, optical properties of AZO are highly dependent on the dimensions and confinement factors of the fabricated structures such as isolated pillars. The extraordinary component of measured permittivity ε_e^{EMA} never becomes negative for both Air/AZO and Si/AZO structures on any frequencies within the characterization range. This implies that the prepared pillars do not support the hyperbolic regime of type-I, although possessing the extremely anisotropic permittivity.

Funding

Villum Fonden (DarkSILD project No. 11116); Direktør Ib Henriksens Fond, Denmark.

Acknowledgments

The authors would like to acknowledge Elena Khomtchenko and Matthias Keil who were responsible for deep-UV stepper lithography. The authors would also like to thank Flemming Bjerg Grumsen for assisting in XRD measurements.